



N, S doped carbon quantum dots inside mesoporous silica for effective adsorption of methylene blue dye

Termeh Teymoorian¹ · Nazanin Hashemi¹ · Mohammad H. Mousazadeh¹ · Zahra Entezarian¹

Received: 7 November 2020 / Accepted: 27 January 2021 / Published online: 10 February 2021

© The Author(s) 2021

Abstract

This study aimed to develop non-metal elements for doping carbon quantum dots (CQDs) with nitrogen and sulfur (N, S-CQDs), which loaded inside hexagonal mesoporous silica (HMS) in order to effectively remove methylene blue dye (MB) from an aqueous solution. The histidine and cysteine amino acids were used as the source for synthesis N, S-CQDs through the hydrothermal method. Morphology and structure of the N, S-CQDs, and adsorbent (N, S-CQDs/HMS) were characterized by using different microscopic and spectroscopic techniques. The adsorption parameters such as adsorbent dosage (0.25–1 g/L), pH (2–10), contact time (15–75 min), and initial MB dye concentration (20–300 mg/L) were investigated. The maximum adsorption capacity and removal efficiency of MB were determined at 370.4 mg/g and 97%, respectively, under optimum conditions at 303 K. The adsorption isotherm studies were fitted with the Freundlich isotherm equation, and the dye removal kinetics of the adsorbent followed the pseudo-second-order model. Thermodynamic studies showed that the adsorption process had exothermic and spontaneous behavior. The removal of MB next to the Rhodamine B and Reactive Black 5 dyes indicated that the N, S-CQDs/HMS had excellent selective behavior for MB absorption. This prepared adsorbent could be well recycled with suitable activity after four repeated adsorption–desorption cycles. Results revealed that the porous characters, surface area, charge properties, reduction in the bandgap, and quantum yield of the N, S-CQDs/HMS were essential factors that affected dye adsorption.

Keyword Carbon quantum dots · Amino acids · Hexagonal mesoporous silica · Adsorption · Methylene blue

Abbreviations

HMS	Hexagonal Mesoporous Silica
CQDs	Carbon Quantum Dots
MB	Methylene Blue
RhB	Rhodamine B
RB5	Reactive Black 5
VDW	Van Der Waals
QY	Quantum Yield
TEOS	Tetraethyl orthosilicate
DDA	Dodecylamine

1 Introduction

Water is one of the vital sources, and water pollution has become the main problem with the rapid growth in the number of industries [1, 2]. Dyes are widely used in many vital industries, such as cosmetics, textiles, plastics, food, etc. [3]. Unfortunately, a considerable amount of dyes are released in running waters without any purification. Many of them are dangerous for humans, animals, and the environment, even at minimal levels [4–6]. Methylene blue (MB) is a kind of dye that is applied in many fields such as textile, biology, medicine, and chemistry. Exposure to MB is harmful to humans, with symptoms such as anemia, vomiting, nausea, and blood pressure. MB absorbs

✉ Mohammad H. Mousazadeh, mousazadeh@aut.ac.ir | ¹Department of Chemistry, Amirkabir University of Technology, 15875-4413 Tehran, Iran.



sunlight, and it causes problems for the growth of aquatic organisms [7]. Hence, the treatment of wastewater containing dyes, especially MB, is crucial. Currently, a variety of treatment ways have been utilized to remove industrial dyes from wastewater, such as photocatalytic and biodegradation, advanced oxidation processes, adsorption, etc. Among all the techniques, adsorption is an effective method that can remove diverse types of contaminants from wastewater due to its highly efficient, sustainable capabilities, and easy-operation [8].

In recent years, carbon quantum dots have attracted more attention rather than other quantum dots because of their fascinating optical properties in biosensors [9], Light-emitting devices [10], drug delivery [11], photocatalysis [12] and, bioimaging [13]. At present, semiconductor quantum dots and water-soluble carbon dots are two kinds of fluorescent-based probes that have attracted more attention and have been studied. Semiconductor quantum dots in contrary to carbon quantum dots, are highly toxic because of their heavy metals like Cd, Te, Se, Pb, etc. So carbon quantum dots are attracted significant interest due to their excellent photostability, optical properties, ease of fabrication, low toxicity, and low-cost synthesis methods [14]. They also can easily functionalize their surface in order to improve their selectivity [15, 16]. Lately, CQDs modified semiconductor materials have been studied for various photocatalytic and electrical applications, for example, CQDs/BiOI [17], CQDs/ZnFe₂O₄ [18], and CQDs/CaTiO₃ [19] nanocomposites. The photodegradation of volatile organic compounds using CQDs/TiO₂ has been rarely studied [20]. Using environmentally friendly and non-metal elements for doping CQDs such as N, S, P, and B can modify fluorescence efficiency and selectivity of the surface due to provide significant functional groups, such as thiol, amine, and carboxyl groups [21, 22]. A few studies demonstrated that the bandgap of CQDs is related to their shape, size, the structure of a surface, and doping with heteroatoms [21]. Moreover, the surface charge and active structure of CQDs altered after heteroatom doping, which has a remarkable impact on the adsorption procedure [23, 24].

The hexagonal mesoporous silica (HMS) belongs to the mesoporous silica nanostructures category. The mesoporous structure has a diameter pore size in the range of 2–50 nm [25]. The pore architecture into the mesoporous silica materials has paramount importance for the utility of these materials. On the other hand, short channels, large pore volumes, and extended pore diameters of HMS would allow more controllable catalyst impregnation and become a more active surface area during a catalysis process rather than other mesoporous materials [26]. The HMS also has other brilliant advantages that are interesting for this research, such as non-toxicity,

low cost, reusability, stability to heat, smaller domain size, and interconnection between its channels. Various excellent performance of the HMS has been proved before, such as catalyst, drug carrier, sensor, and adsorbent [27–29].

Herein, we employed a hydrothermal method to synthesize N, S–CQDs with eco-friendly and non-metal elements for doping CQDs from cysteine and histidine amino acids as a source of nitrogen and sulfur elements. The N, S–CQDs were encapsulated in the HMS channels during the sol–gel process for effective adsorption of methylene blue dye. The N, S–CQDs were characterized using the UV-Vis, PL, DLS, FT-IR, and zeta potential technique. The surface characterization of the adsorbent was investigated by using FT-IR, FESEM, EDX, BET, and XRD techniques. The isotherm equilibrium, kinetic, and thermodynamics of the adsorption were studied.

2 Materials and methods

2.1 Materials

All chemicals were used without further purifications and employed as received. L-Histidine ($\geq 99\%$), L-Cysteine ($\geq 98\%$), and Tetraethyl orthosilicate (TEOS; $\geq 99\%$) were all purchased from Sigma Aldrich Chemical Co. Dodecylamine (DDA; 95%) was purchased from Fluka (Shanghai, China). Methylene Blue (C₁₆H₁₈ClN₃S, MW: 319.85 g mol⁻¹, $\lambda_{\max} = 664$ nm), Rhodamine B (C₂₈H₃₁ClN₂O₃, MW: 479.01 g mol⁻¹, $\lambda_{\max} = 562$ nm), and Reactive Black 5 (C₂₆H₂₁N₅Na₄O₁₉S₆, MW: 991.82 g.mol⁻¹, $\lambda_{\max} = 596$ nm) were purchased from Merck chemical Co.

2.2 Synthesis of N, S co-doped CQDs

The hydrothermal method was used to synthesis N, S co-doped CQDs. 0.6 gr of l-histidine with 0.12 gr of l-cysteine was diluted and dispersed for several minutes in 18 ml of deionized water. The solution was transferred into 30 ml of Teflon autoclave and heated up to 180 °C for about 10 h. The solution changed from colorless to brown during the reaction. The final product was separated from larger particles with centrifuging at 12,000 rpm for 20 min [30]. The same procedure was utilized to synthesize N doped CQDs (using histidine amino acid) to compare with N, S co-doped CQDs.

2.3 Synthesis of N, S-CQDs inside HMS (N, S-CQDs/HMS)

To synthesize the N, S-CQDs/HMS, 1 ml of N, S-CQDs dissolved in 135 ml deionized water and 17.6 ml Ethanol. At the next step, 11.5 ml of TEOS as a silica precursor was

added slowly to the solution. Then 1.85 gr of DDA as the structure-directing performer was added and dissolved in the mixture under vigorous stirring. The stirring continued for 24 h. The precipitated material was then filtered and washed with deionized water. The sample was dried for 1 day at 90 °C in the oven and finally calcined at 450 °C for 30 min. The same procedure was utilized for synthesizing pure HMS and N-CQDs/HMS to compare with N, S-CQDs/HMS.

2.4 Adsorption experiments

The adsorption experiments were performed under different conditions for optimization, pH: 2–10, the dosage of adsorbent: 0.25–1.00 g/L, contact time: 15–75 min, and initial MB concentration: 20–300 mg/L. The dye solution was contacted with a specified amount of N, S-CQDs/HMS under stirring by using a magnetic stirrer with a speed of 500 rpm. 0.1 M NaOH and 0.1 M HCl solution were utilized to adjust the pH solutions. For investigating the selectivity property, the N, S-CQDs/HMS was individually added to combined solutions of the 20 ppm MB-RhB and MB-RB5 under optimized conditions. After the adsorption process, the residual dye concentration was determined using UV-Vis spectroscopy at the maximum wavelengths of 664 nm for the MB, 562 nm for the RhB, and 596 nm for the RB5. The removal efficiency ($R\%$) and the equilibrium capacity q_e (mg/g) of the dye were computed by Eqs. (1) and (2) [31, 32]:

$$R\% = \frac{(C_0 - C_e)}{C_0} \times 100 \quad (1)$$

$$q_e = (C_0 - C_e) \times \frac{V}{m} \quad (2)$$

where C_0 and C_e (mg/L) are the initial and equilibrium concentrations of adsorbate in the solution, V (L) is the volume of dye solution used, and m (g) is the weight of the adsorbent.

2.5 Characterization

The optical properties of the N, S-CQDs were determined by UV-Vis spectroscopy (Perkin Elmer lambda 45) and fluorescence spectroscopy (PL) (Perkin Elmer LS55). The particle size and surface charge of the S, N-CQDs were determined by dynamic light scattering (DLS) and zeta potential (Horiba SZ100). The surface morphology of the N, S-CQDs/HMS was investigated by using Field Emission Scanning Electron Microscope (FESEM) (TESCAN, MIRA III). Fourier transform spectroscopy (FT-IR) (Bruker, alpha) was used to determine the main functional groups of the N, S-CQDs,

and adsorbent between 400 and 4000 cm^{-1} wavelengths by using the KBr pellet technique. The crystallographic structure of the adsorbent was analyzed using X-Ray diffraction (XRD). The Brunauer–Emmett–Teller (BET) method was utilized to determine the specific surface areas, pore-volume, and pore size. Elemental composition analysis of the N, S-CQDs/HMS was done using X-ray energy dispersive spectroscopy (EDS) (Scheme 1).

2.6 Calculation of quantum yield (QY)

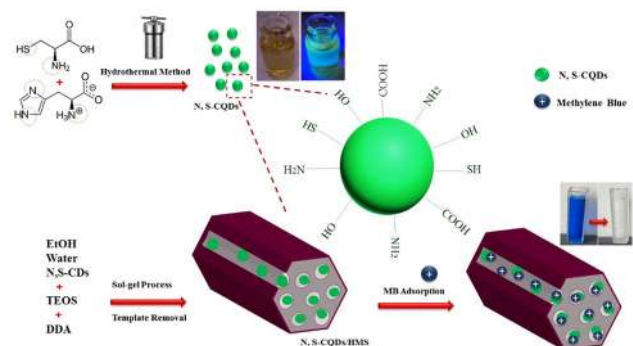
The QY of CQDs was obtained based on Eq. (3). Quinine sulfate in 0.5 M H_2SO_4 was applied as a reference with a known QY amount of 54% at 350 nm excitation wavelength.

$$QY_{CQDs} = QY_R \left(\frac{A_R}{A_{CQDs}} \right) \left(\frac{I_{CQDs}}{I_R} \right) \left(\frac{\eta_{CQDs}}{\eta_R} \right)^2 \quad (3)$$

where, QY is the quantum yield, A is the optical density, I is the integrated fluorescence intensity, and η is the refractive index of solvent ($\eta_{CQDs} = 1.33$ and $\eta_R = 1.76$). In this experiment, the solvent of the CQDs and the reference substance were water and 0.5 M H_2SO_4 in water, respectively. The subscript "R" and "CQDs" refers to reference substance (Quinine sulfate) and CQDs sample.

3 Results and discussion

Figure 1 compares the adsorption capacity and adoption efficiency of 3 different adsorbents (HMS, N-CQDs/HMS, N, S-CQDs/HMS) for MB dye removal in the same conditions. The experiment results revealed that 97% of MB (20 mg/L) was adsorbed on the surface of the N, S-CQDs/HMS composite within 45 min. However, the HMS could only adsorb 70% of MB, and for N-CQDs/HMS was 80% under the same conditions. These results revealed that the N, S-CQDs/HMS



Scheme 1 Synthesis routes of N, S-CQDs/HMS, and adsorption of Methylene blue dye

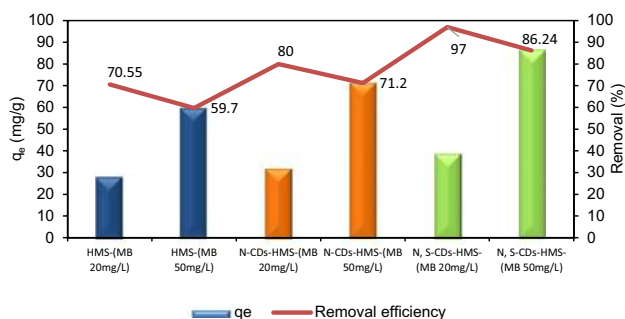


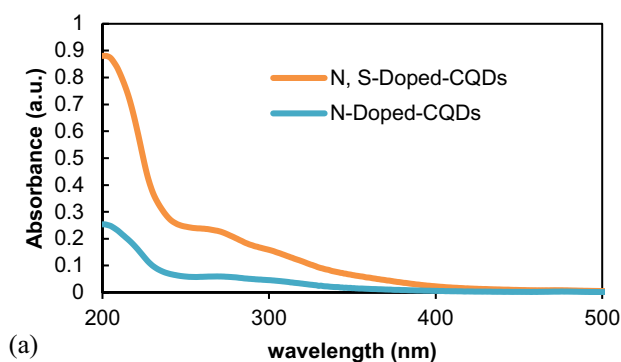
Fig. 1 Adsorption condition: $C_0=20\text{--}50$ mg/L, adsorbent dosage=0.5 g/L, pH=7, time=45 min

composites displayed higher adsorption activities than N-CQDs/HMS. The attachment of both N and S atoms on CQDs that loaded in the HMS surface facilitated the bonding formation between adsorbent and MB dye, which will be discussed in the characterization part of this article, and it was chosen as the preferred adsorbent for further experiments.

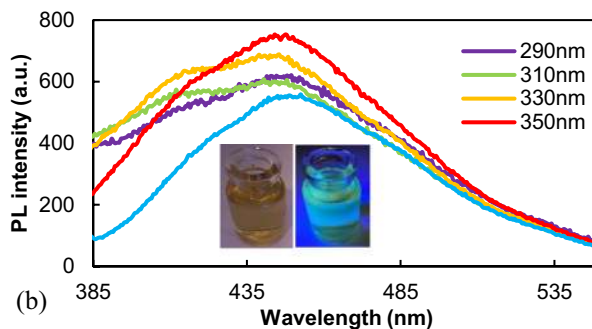
3.1 Characterization

Optical properties of the N, S-CQDs, and N-CQDs were investigated by UV-Vis and photoluminescence (PL) spectroscopy. Figure 2a represents the UV-Vis absorption of CQDs solutions. A specific absorption peak at ~268 nm related to the $\pi\text{-}\pi^*$ transition of electrons in the conjugated C=C band, and adsorption peak at 300~350 nm assigned to the $n\text{-}\pi^*$ transition of C=N, C-N, C=S, and C=O bonds [21, 33, 34]. The low-intensity absorption of $n\rightarrow\pi^*$ is ascribed to the lower content and weak electron transition of the functional groups in CQDs. The PL emission of the N, S-CQDs was dependent on the excitation wavelength. The excitation wavelengths were increased from 290 to 370 nm, and the maximum emission peak was seen at 447 nm with an excitation wavelength of 350 nm (Fig. 2b) [33]. The fluorescence mechanism of N, S-CQDs under varied excitation wavelengths, is shown in Fig. 2c. The N doped CQDs had strong fluorescence effects in blue-shift, while N, S doped CQDs had exhibited redshift [35, 36]. The presence of S heteroatom may result in higher PL properties. The fluorescence spectra of the N, S-CQDs, and N-CQDs solutions demonstrated a strong emissions peak located at 447 and 442 nm, respectively, with an excitation of 350 nm (Fig. 2d).

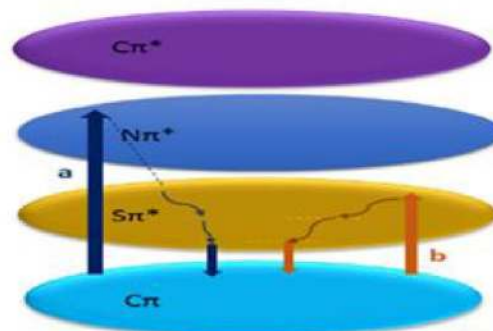
The presence of Sulfur within N-CQDs brings S-related levels of energy among π and π^* of the carbon atom. The resulting extra levels of energy propel multiple emission peaks to illustrate the redshift emission of N, S-CQDs. The excited electrons jumped inside upper levels of energy under the short wavelengths of excitation. After vibration



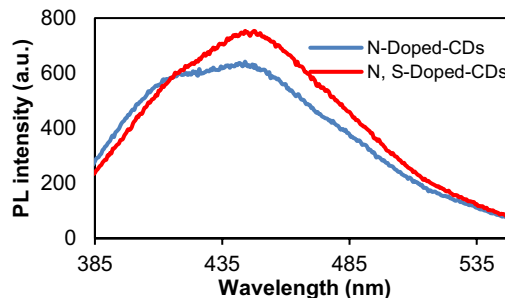
(a)



(b)



(c)



(d)

Fig. 2 a UV-Vis absorption spectra of N-CQDs and N, S-CQDs b PL emission of the N, S-CQDs under different excitation wavelengths c The fluorescence mechanism of N, S-CQDs under varied excitation wavelengths d PL emission curves of N-CQDs and N, S-CQDs excited at 350 nm

relaxation and passes through the band, the radiant recombination will then occur on $S\pi^*$ and cause independent excitation of the orange luminescence (Fig. 2c, path a). In the path b, the transition electron was transported through at lower levels of energy by growing excitation wavelength. The orange luminescence was emitted immediately after vibrational relaxation, with no further crossing interband [22].

The size and the composition of the surface influence the bandgap of CQDs and explain the complication of the PL method [37]. The emissions of N, S-CQDs were significantly redshifted from 442 to 447 nm, which can be associated with surface defects caused by C-N and C-S groups into the CQDs. Based on UV information (Fig. 2a), the bandgap energy of CQDs computed by the following equation:

$$\alpha h\nu = A(h\nu - E_g)^{\frac{1}{2}} \quad (4)$$

where α , h , ν , A , and E_g are the coefficient of the absorption, Planck constant, photon's frequency, constant, and bandgap energy, respectively. The bandgap value of the N, S-CQDs, and N-CQDs were computed to be 3.3 and 3.7 eV, respectively. This reduced value of the N, S-CQDs bandgap in comparison with the N-CQDs, originated from the results of co-doped with S and N elements [38]. Since the π orbital has emanated from the HOMO orbital and π^* is actually the LUMO orbital with antibonding nature, it is logical that having HOMO and LUMO of orbitals near to each other, helps the π^* to compel its antibonding nature over bonding π orbital more effectively. In other words, when LUMO is near to HOMO, they have interactions more effectively, and LUMO can have more effective destructive interference with the π orbital.

The particle size of the N, S-CQDs was determined around 8 nm by using the DLS measurement (Fig. 3). The surface charge of the N, S-CQDs, and N-CQDs were

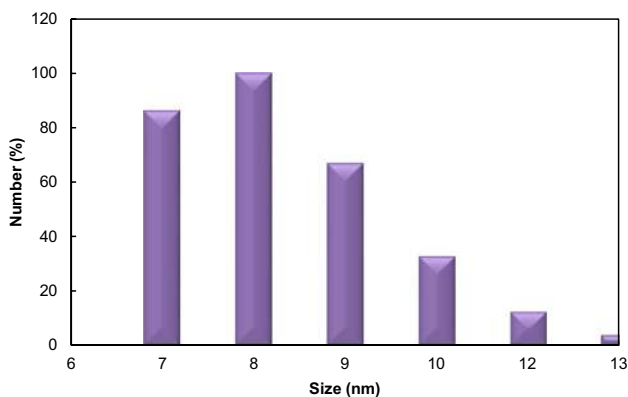


Fig. 3 The size distribution of N, S-CQDs obtained through DLS measurement

determined as -30.7 and -5.3 mV at pH = 7, respectively, hence N, S-CQDs can adsorb positively charge dyes like MB better than N-CQDs (Table 1). The N, S-CQDs have a more negative charge due to the presence of $-SH$ groups. The zeta potential is very sensitive in different pH; at the pH higher than seven, the zeta potential mainly continues negative, and at the acidic pH, it turns into zero to the positive charge [39]. The quantum yield (QY) of each CQDs were computed and exhibited in Table 1. The QY was found for N, S-CQDs, and N-CQDs, 60.8%, and 41.6%, respectively. These results demonstrated that the structure of amino acids could effectively influence the optical properties of the synthesized CQDs, such as PL intensity and QY. The FESEM images indicated the pore and spherical structure of the N, S-CQDs/HMS, and pure HMS (Fig. 4). Irregular particles gained mainly due to merge inside each other randomly during the synthesis [40].

The FTIR spectra of the N, S-CQDs, and adsorbent (N, S-CQDs/HMS) are shown in Fig. 5a, b. Appearing The new peaks of N, S-CQDs at 1629, 1460, 1401, 1224, and 1023 cm^{-1} can be allocated to C=N, C-H, C-N, C=O and C-O bonds, respectively. The broadband at 3145–3429 cm^{-1} is assigned to O-H and N-H bonds. The peaks of 690 cm^{-1} at lower wavenumbers are ascribed to C-S bonds. In comparison, the FTIR spectrum of N, S-CQDs/HMS showed the broadband at 3700–3100 cm^{-1} that were attributed to O-H, N-H bonds, and appearing an adsorption band at 1637, 1729 and around 1010 cm^{-1} corresponded to the C=N, C=O and bending vibrations of C-O-C of CQDs. Figure 5b indicates that the CQDs had been successfully loaded on the HMS [22, 27, 41]. The results exhibited that N and S atoms were effectively doped within the carbon framework of CQDs/HMS, which has been confirmed with the EDS analysis. The elemental analysis (EDS) confirms the elements of the N, S, C, O in the N, S-CQDs/HMS (Fig. 6a). The atomic ratio of the O/C/N/S is determined to be 79.5/14.0/6.0/0.36, respectively, which confirmed the co-doping of CQDs with both N and S atoms. The N and S co-doping within the conjugated carbon skeleton of CQDs modified its electronic behavior, the chemical properties of the surface, and the intensity of PL, which have significant competency for the efficient removal of various cationic dyes.

The XRD patterns exhibited that the HMS structure is well retained even after incorporating N, S-CQDs species

Table 1 Zeta potential and quantum yield results of N-CQDs and N, S-CQDs

Carbon dots	Zeta potential (mV)	QY%
N-CQDs	-5.3	41.6
N, S-CQDs	-30.7	60.8

Fig. 4 FESEM image of **a** HMS
b N, S-CQDs/HMS adsorbent

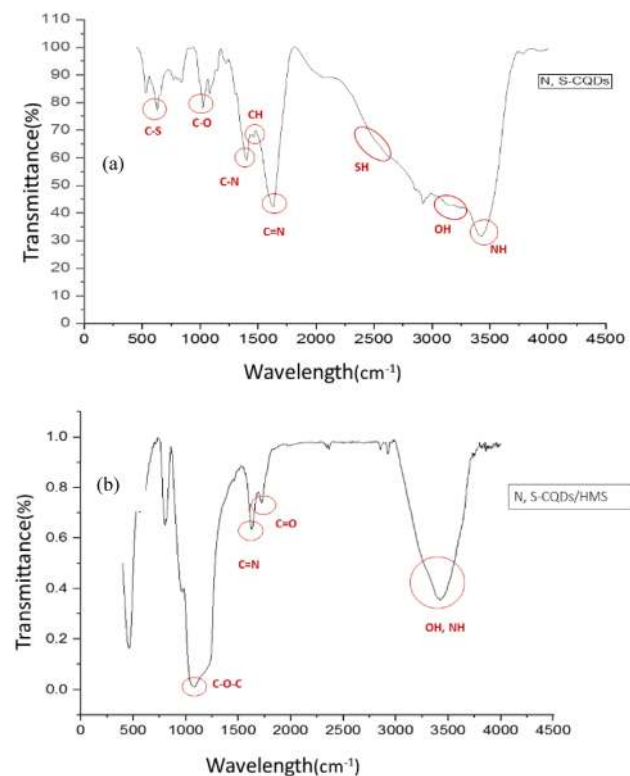
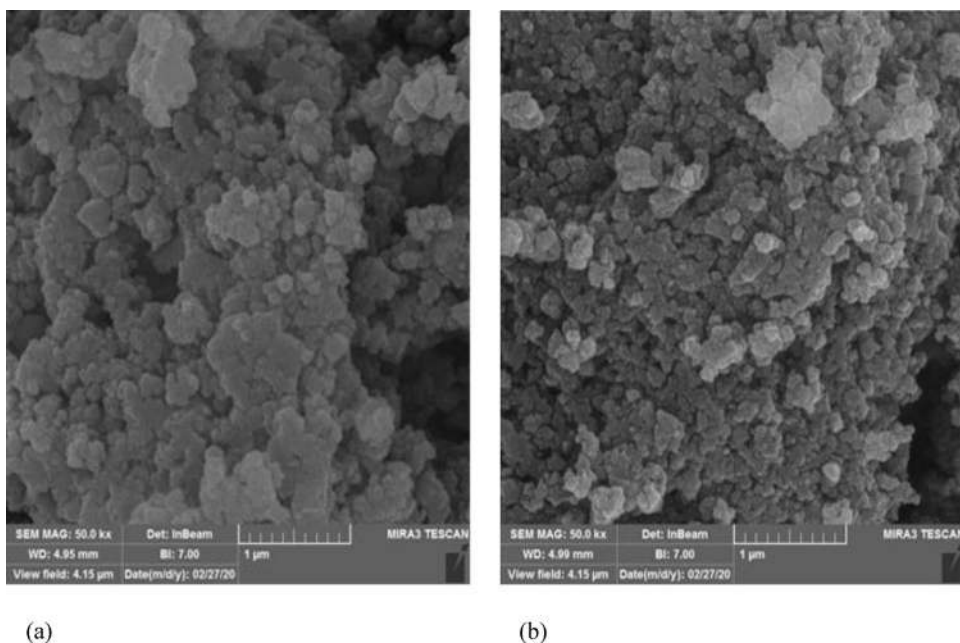


Fig. 5 Fourier-transform infrared spectra of **a** N, S-CQDs **b** N, S-CQDs/HMS

(Fig. 6b and c). The adsorbents exhibit distinct diffraction peaks at $2\theta = 2.5^\circ$, which is characteristic of the HMS structure. No diffraction peaks related to agglomerated CQDs can be observed; hence, we can assume that the CQDs are

dispersed uniformly and incorporated inside the structure of the HMS in a noncrystalline manner or very small crystalline components. The low crystallinity is essential for the adsorbent activity of the adsorbent since it can expand the active surface of the adsorbent [41, 42]. The adsorbents showed a broad peak around $2\theta \sim 26^\circ$, which is commonly attributed to the amorphous peak of the HMS framework. With the incorporation of the N, S-CQDs components, the broad peak of amorphous HMS becomes a little sharper; these results suggest that the N, S-CQDs is doped in HMS species and do not have bulky crystals of CQDs (Fig. 6c) [41, 43]. The BET results (Table 2) show that the surface area, average pore size, and volume of the HMS increased with adding N-CQDs and N, S-CQDs in the mesoporous structure of the HMS, which suggested that the CQDs were assembled into the inner wall of mesopores rather than inside the pores, therefore, confirmed the DLS measurements. The pore size distribution also increased from 0.69 to 1.37 cm^3/g , exhibit its better adsorption than HMS [44, 45].

3.2 Effect of pH

pH is one of the significant parameters that influence the surface charge of the adsorbent and dye. The pH was adjusted with diluted HCl and NaOH solutions in the range of 2–10. Figure 7a shows the effects of the pH on the adsorption of MB by adsorbent in the other constant parameters (time: 45 min, temperature: 30 °C). The adsorption process was increased by increasing the pH value. The pH in the range of 7–10 was confirmed to the best effective value to adsorb cationic MB due to the existence of

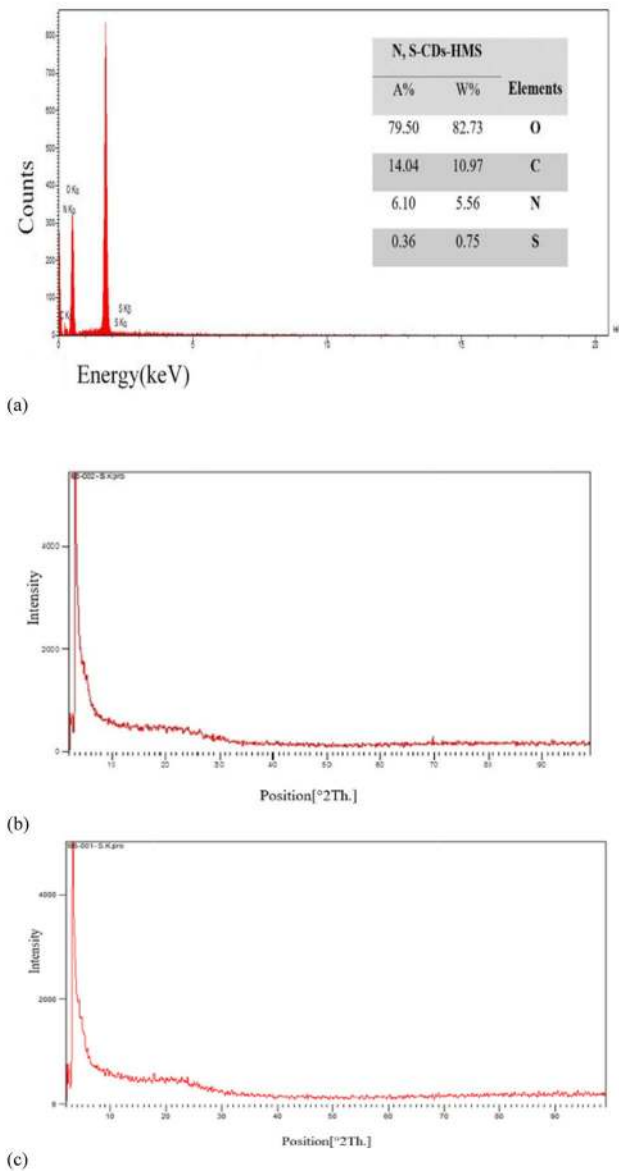


Fig. 6 a EDS analysis of N, S-CQDs/HMS b X-ray diffraction of HMS; c X-ray diffraction of N, S-CQDs/HMS

Table 2 BET results of HMS, N-CQDs/HMS, and N, S-CQDs/HMS

Sample	S _{BET} (m ² /g)	Pore diameter (nm)	Pore volume (cm ³ /g)
HMS	910	2.30	0.69
N-CQDs/HMS	1274	2.45	0.93
N, S-CQDs/HMS	1491	2.45	1.37

a negative charge on the surface of the N, S-CQDs/HMS. Hence pH = 7 was selected as the optimized pH for further investigations.

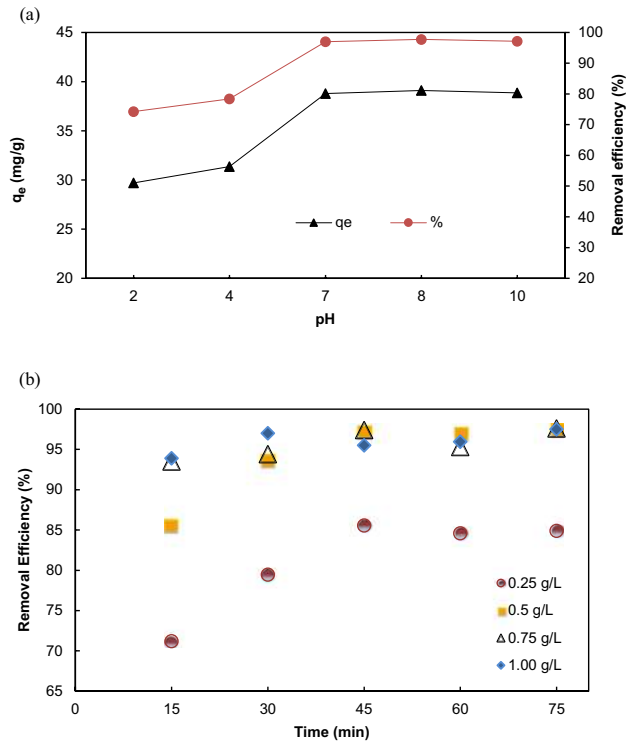


Fig. 7 a Effects of pH b Effect of time and dosage of N, S-CQDs/HMS on the MB adsorption

3.3 Effects of adsorbent dosage and time

Figure 7b demonstrates the effect of the different dosages of N, S-CQDs/HMS (0.25–1.0 g/L) under the contact time between 15 to 75 min. The results indicated that the adsorption capacity decreased with an increase in the adsorbent amount. However, the removal efficiency increased with increasing the adsorbent dosage from 0.25 to 0.50 g/L due to enhancement in the active sites of the surface. The result also indicated that more amount of the adsorbent after 0.50 g/L did not change significantly for the dye removal efficiency after 45 min.

3.4 Effects of dye concentration and isotherm studies

The effect of different MB concentrations (20–300 mg/L) at temperatures ranging between 303 and 343 K on the adsorption process is demonstrated in Fig. 8a. The adsorption capacity of the N, S-CQDs/HMS was significantly dependent on the initial concentrations of MB in the solution; When the MB concentration increased, the adsorption sites on the surface of N, S-CQDs/HMS became saturated. The adsorption isotherm models were employed to give essential information in designing adsorption systems. In this research, the Langmuir,

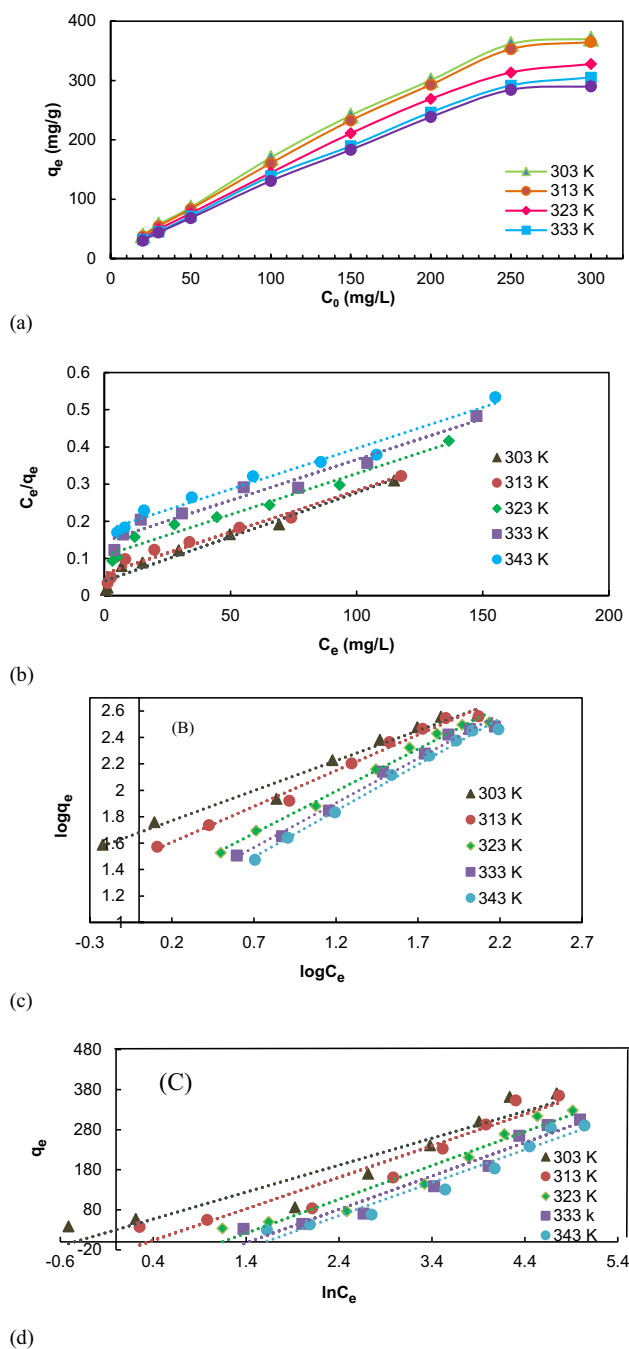


Fig. 8 a Effect of MB dye concentration on the adsorption by N, S-CQDs/HMS b Langmuir c Freundlich d Temkin isotherm models for the MB adsorption by N, S-CQDs/HMS

Freundlich, and Temkin isotherm models were selected to analyze the equilibrium data (Fig. 8b, c, d). The Langmuir model demonstrates monomolecular layer adsorption with a specific number of sites on the homogenous surface with no interaction between adsorbed particles. The Langmuir isotherm could be based on Eq. (5):

$$\frac{C_e}{q_e} = \frac{1}{q_m K_L} + \frac{C_e}{q_m} \tag{5}$$

where C_e (mg/L) and q_e (mg/g) related to the equilibrium concentration of MB dye and the adsorbed of MB per unit mass of the adsorbent, respectively. The equilibrium capacity (q_m) is described as the maximum adsorption capacity, and K_L is the Langmuir constant.

The Freundlich model assumes that the adsorption accrues in the heterogeneous and multilayer surface of the adsorbent with diverse energies. This isotherm model was applied in the following form:

$$\log q_e = \log k_f + \frac{1}{n_f} \log C_e \tag{6}$$

K_f and $1/n_f$ are Freundlich constant and adsorption intensity, respectively. The n_f value in the range of 1–10 supports favorable adsorption behavior [2, 4, 46]. The highest correlation coefficient value of this model demonstrates a suitable fit among the other models.

Temkin isotherm supposes that the heat of adsorption reduces linearly due to interactions between adsorbent and adsorbate. The Temkin isotherm model offered in the following Eq. (7):

$$q_e = B \ln K_T + B \ln C \tag{7}$$

where $B = (RT/b_T)$ constant related to the heat of sorption (J/mol), b_T is Temkin isotherm constant, and K_T (L/g) is Temkin isotherm equilibrium binding constant, which is an indication of the maximum binding energy [47].

The isotherm parameters and constants are calculated in Table 3. According to the correlation coefficient value, the Freundlich and Langmuir isotherm models were the best fit for the adsorption process, respectively. The Freundlich constant was calculated 2.02, 1.84, 1.56, 1.48, and 1.43, with increasing temperature from 30 to 70 °C, respectively. The results indicated the desirability of the adsorption procedure.

3.5 Effects of temperature and thermodynamic studies

In order to evaluate the effects of the temperature and thermodynamics behaviors of the dye adsorption process, the equilibrium data was measured by using the Eqs. (8, 9, 10) [48, 49]:

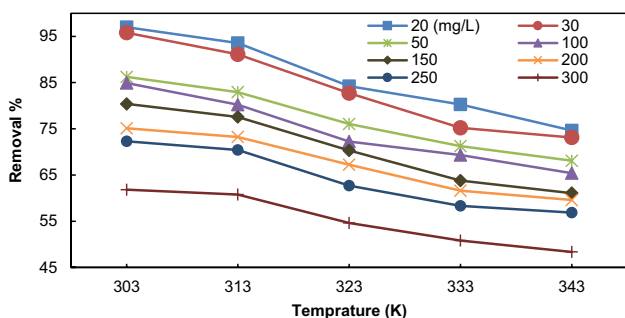
$$\Delta G = -RT \ln K_D \tag{8}$$

$$\Delta G = \Delta H - T \Delta S \tag{9}$$

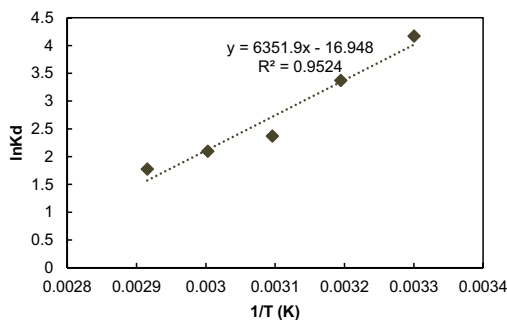
K_D is described as follow:

Table 3 Isotherm parameters for the MB adsorption by N, S-CQDs/HMS

Isotherm model	Parameters	Units	Temperature				
			303 K	313 K	323 K	333 K	343 K
Langmuir	R^2	–	0.9666	0.9638	0.9726	0.9631	0.9739
	q_{max}	mg/g	416.66	454.54	454.54	454.54	454.54
	K_L	L/mg	0.061	0.037	0.020	0.015	0.012
Freundlich	R^2	–	0.9777	0.9873	0.9889	0.9881	0.9914
	K_f	$(\text{mg}\cdot\text{g}^{-1})$ $(\text{L}\cdot\text{mg}^{-1})^{1/n}$	47.81	31.48	16.86	12.47	10.15
	n_f	–	2.202	1.842	1.566	1.484	1.432
Temkin	R^2	–	0.9039	0.9216	0.947	0.9438	0.9521
	K_T		1.563	0.703	0.319	0.240	0.200
	B	J/mol	67.195	78.677	84.291	83.337	82.289



(a)



(b)

Fig. 9 a Effect of temperature on the MB adsorption by N, S-CQDs/HMS b Van't hoff regression of MB adsorption

$$K_D = q_e C_e^{-1} \tag{10}$$

as shown in Fig. 9a, with increasing the temperature from 303 to 343 K, the MB removal efficiency was decreased gradually at different initial concentrations. The values of thermodynamic parameters for the adsorption of MB ($C = 20$ mg/L) are given in Table 4. The Gibbs free energy changes (ΔG) indicates the spontaneous procedure of the MB adsorption without external energy when the temperatures were in the range of 30–70 °C. The negative value of ΔH displays the exothermic nature of the adsorption procedure (Fig. 9b). The negative amount of ΔS indicated decreased randomness at the solid/solution interface during the process of sorption [50, 51]. The negative values of ΔH and ΔS showed that hydrogen bonds and VDW force were the principal forces governing binding in the MB-CQDs/HMS system [45].

3.6 Kinetics of adsorption

Kinetics studies were applied to investigate the mechanism and effects of contact time on the dye adsorption. The experimental data was controlled by using the pseudo-first-order (PFO) and pseudo-second-order (PSO) models which their equations are as follow respectively: (Eqs. (11)-(12)) [52]:

Table 4 Thermodynamics parameters for the MB adsorption by N, S-CQDs/HMS

Sample	ΔS ($\frac{\text{J}}{\text{mol}\cdot\text{K}}$)	ΔH ($\frac{\text{kJ}}{\text{mol}}$)	R^2	ΔG ($\frac{\text{kJ}}{\text{mol}}$)	Temperature	
					T/K	T/°C
N, S-CQDs/HMS	– 140.90	– 52.80	0.9524	– 10.10	303	30
				– 8.76	313	40
				– 6.36	323	50
				– 5.80	333	60
				– 5.05	343	70

Table 5 Kinetics parameters for the MB adsorption by N, S-CQDs/HM

Kinetics model	units	Parameters	N, S-CQDs/HMS
PFO	R^2	–	0.0910
	k_1	1/min	0.085
	q_e	mg/g	16.180
PSO	R^2	–	0.9997
	k_2	g/mg min	1.05×10^{-5}
	q_e	mg/g	40.322

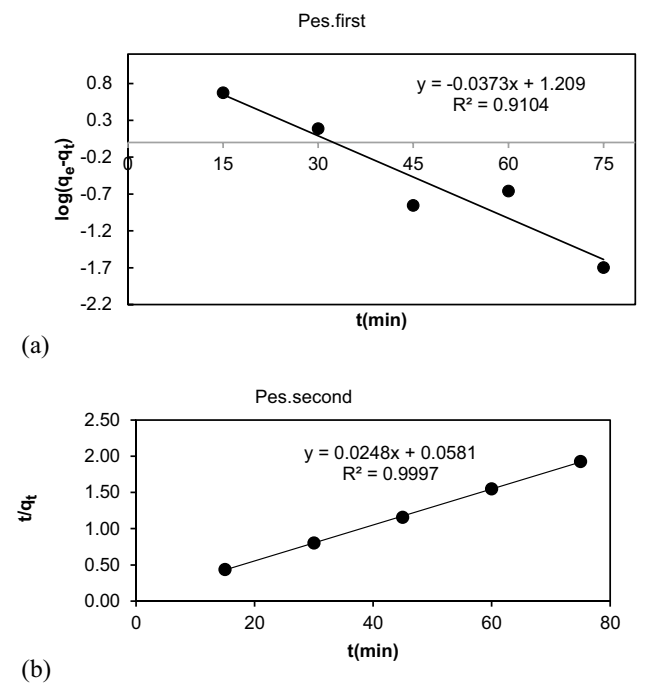


Fig. 10 Kinetics models for the MB adsorption by N, S-CQDs/HMS

$$\log(q - q_t) = \log q_e - \frac{K_1 t}{2.303} \tag{11}$$

$$\frac{t}{q_t} = \frac{1}{K_2 q_e^2} + \frac{t}{q_e} \tag{12}$$

where q is the equilibrium adsorption capacity (mg/g), q_t is the dye concentration on adsorbent at time t (mg/g), q_e is the theoretical equilibrium adsorption capacity (mg/g), K_1 is the rate constant of pseudo-first-order adsorption (1/min), t is the time (min), and K_2 is the rate constant of pseudo-second-order adsorption (g/mg.min). Experimental results (Table 5) revealed that the MB adsorption by the N, S-CQDs/HMS follows the PSO model due to the high correlation coefficient (R^2) values. Figure 10 indicates that the pseudo-second-order model can be the best model to describe the MB adsorption on the surface of the N,

S-CQDs/HMS, which suggests that the adsorption procedure is involving the electrostatic interaction among the cationic part of the MB dye and negatively charged available groups on the adsorbent surface[53, 54].

3.7 Selectivity

N, S-CQDs/HMS was individually added to a solution, including MB-RhB or MB-RB5, with equal concentrations. As demonstrated in Fig. 11, after 45 min, the MB-RhB solution turned from dark blue to light pink color, and the MB-RB5 solution changed from dark blue to light blue color. For the mixture of MB-RhB, the N, S-CQDs/HMS demonstrated higher adsorption for cationic MB than cationic RhB; this is due to the larger size and steric hindrance of RhB. For the mixture of MB-RB5, it can be explained that the MB has a cationic charge, whereas RB5 is anionic; therefore, MB can be adsorbed through electrostatic interaction with the anionic adsorbent. After the adsorption of cationic MB onto the surface of the adsorbent, the RB5 dye was further adsorbed due to the charge influences. The structures of MB, RhB, and RB5 dyes are illustrated in Fig. 12.

3.8 Regeneration studies

Reusability of the N, S-CQDs/HMS in the MB removal was investigated for four consecutive cycles. After each run, the adsorbent was separated by centrifugation, washed several times by ethanol for desorption, and dried at 80 °C for 10 h. The recycled solid was used for the next run. The removal efficiency for the first time was 94.79% and then declined to 82.73% in the fourth cycle. The results indicated that the N, S-CQDs/HMS had a suitable reusability performance after four adsorption–desorption cycles (Fig. 13). The maximum adsorption capacity of the N, S-CQDs/HMS in the adsorption of methylene blue from aqueous solutions was 370.4 mg/g, which was compared to the other reported adsorbents (Table 6).

4 Conclusion

The novel N, S-CQDs/HMS adsorbent was successfully synthesized as an effective adsorbent to remove cationic MB dye from the aqueous solution. Biocompatible histidine and cysteine amino acids were used as the source of N, S doped-carbon dots. The surface morphology, crystalline structure, chemical composition, optical property, and sorption behavior for N, S-CQDs/HMS were all characterized. It was found that the structure of starting materials can effectively influence the optical properties (PL intensity and quantum yields), and it caused

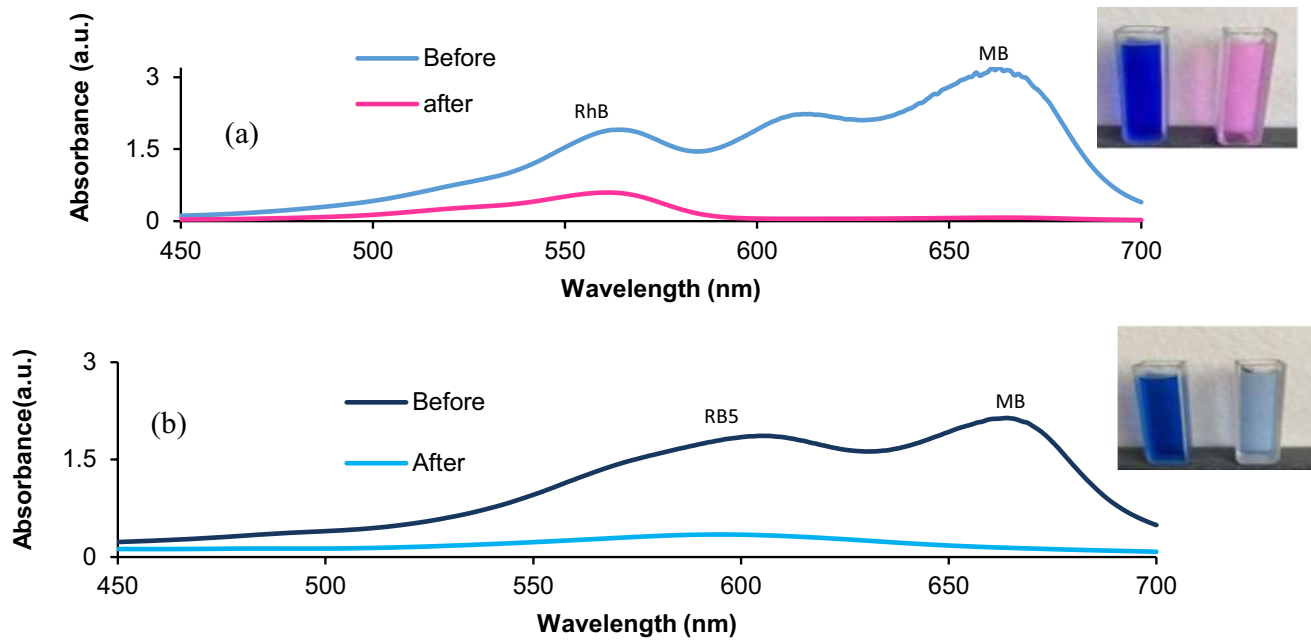
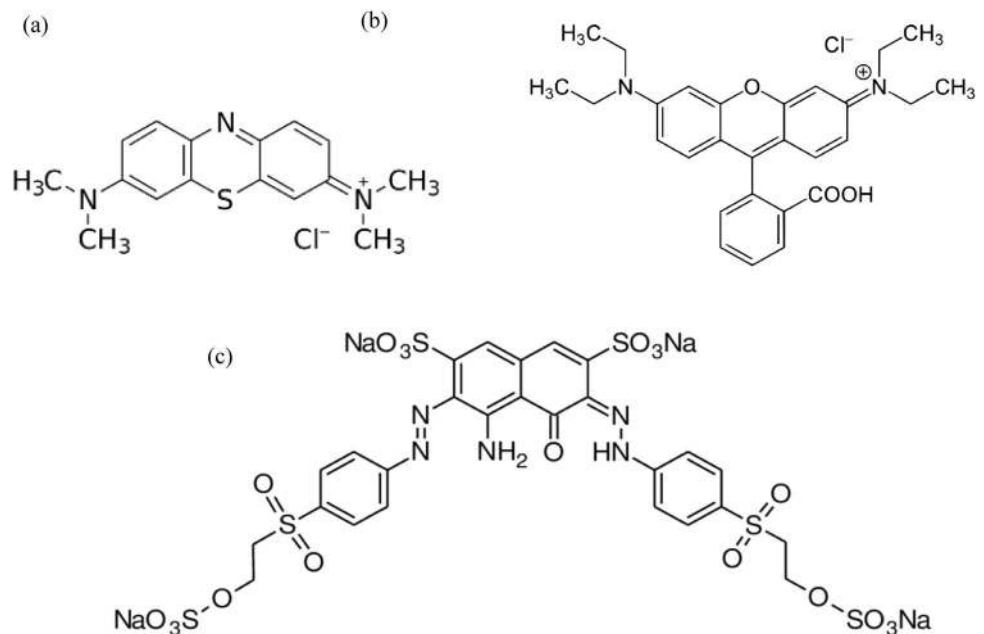


Fig. 11 Selective adsorption of N, S-CQDs/HMS for **a** MB-RhB **b** MB-RB5 solutions

Fig. 12 Chemical structure of **a** Methylene Blue **b** Rhodamine B **c** Reactive Black 5



better dye absorption. Furthermore, having HOMO and LUMO close together in a small bandgap system of N, S-CQDs will increase π and π^* interactions and facilitates the dye adsorption process. The removal efficiency and adsorption capacity of MB were obtained at 97% and 370.4 mg/g, respectively. The equilibrium data showed proper fitting to the pseudo-second-order kinetic and the Freundlich isotherm models. The thermodynamic parameters validated the spontaneity and exothermic

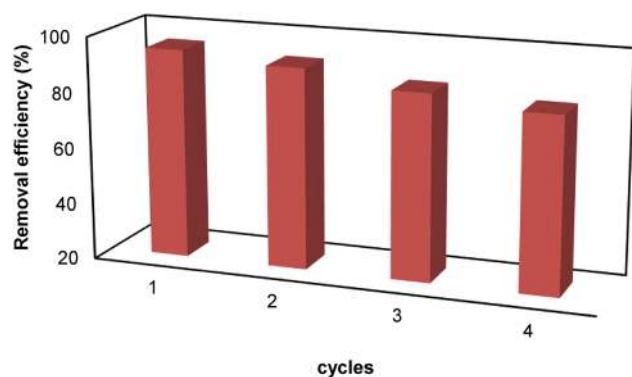


Fig. 13 Reusability of N, S-CQDs/HMS in the MB removal by running four adsorption – desorption cycles

nature through the dye adsorption process. The removal of MB next to the RhB and RB5 dyes indicated that the N, S-CQDs/HMS had excellent selective action for MB absorption. Also, this adsorbent could be well recycled with suitable activity after four repeated cycles. Therefore, N, S-CQDs/HMS is an excellent promising adsorbent due to its metal-free, cost-effective, eco-friendly nature,

high surface area, reusability, and selective performance for adsorption of cationic MB dye from aqueous solution, especially where centralized wastewater treatment facilities are not accessible.

Acknowledgement The authors acknowledge the Amirkabir University of Technology (Tehran, Iran) for the financial support of this work.

Compliance with ethical standards

Conflict of interest The authors declare no competing financial interest.

Open Access This article is licensed under a Creative Commons Attribution 4.0 International License, which permits use, sharing, adaptation, distribution and reproduction in any medium or format, as long as you give appropriate credit to the original author(s) and the source, provide a link to the Creative Commons licence, and indicate if changes were made. The images or other third party material in this article are included in the article's Creative Commons licence, unless indicated otherwise in a credit line to the material. If material is not included in the article's Creative Commons licence and your intended use is not permitted by statutory regulation or exceeds the permitted use, you will need to obtain permission directly from the copyright holder. To view a copy of this licence, visit <http://creativecommons.org/licenses/by/4.0/>.

Table 6 Maximum adsorption capacities for the adsorption of MB on a variety of adsorbents

Adsorbent	Maximum Adsorption Capacity (mg/g)	References
Activated carbon from coconut coir	15.5	[55]
Sugar Scum	24.5	[56]
Graphene oxide–cellulose nanowhisker	34.5	[57]
Acid-functionalized biosorbent	50.6	[58]
Ag/SiO ₂	55	[59]
Mesoporous SiO ₂ nanoparticles decorated with SnO ₂ quantum dots	73.1	[60]
Mesoporous titania (TiO ₂)—polyvinyl alcohol (PVA) nanocomposite	138.8	[61]
Carbonaceous adsorbent from corncob	140.2	[62]
Mesoporous Iraqi red kaolin clay	240.4	[63]
Mesoporous activated carbon from bamboo chip	305.3	[64]
N, S-CQD/HMS	370.4	This work

References

1. Khatoun J, Shah MR, Malik MI, Khan IAT, Khurshid S, Naz R (2019) Convenient pH-responsive removal of Acid Black 1 by green l-histidine/iron oxide magnetic nanoadsorbent from water: performance and mechanistic studies. *RSC Adv* 9(6):2978–2996
2. Wu MZ, Shi JY, Chen PY, Tian L, Chen J (2019) Two 3D cobalt (II) metal-organic frameworks with micropores for selective dye adsorption. *Inorg Chem* 58(5):3130–3136
3. Kulasooriya T, Priyantha N, Navaratne A (2020) Removal of textile dyes from industrial effluents using burnt brick pieces: adsorption isotherms, kinetics and desorption. *SN Appl Sci* 2(11):1–11
4. Duo H, Tang H, Ma J, Lu X, Wang L, Liang X (2019) Iron-based metal-organic framework as an effective sorbent for the rapid and efficient removal of illegal dyes. *New J Chem* 43(38):15351–15358
5. Tuzen M, Sari A, Saleh TA (2018) Response surface optimization, kinetic and thermodynamic studies for effective removal of rhodamine B by magnetic AC/CeO₂ nanocomposite. *J Environ Manage* 206:170–177
6. Al Subhi A, Valizadeh Kiamahalleh M, Firouzi M, Yousefi F, Kyaw HH, Al Abri M et al (2020) Self-assembled graphene hydrogel composites for selective dye removal. *Adv Sustain Syst* 4:2000055
7. Goudarzi MG, Bagherzadeh M, Taheri F, Rostami-Vartooni A (2020) Preparation and characterization of magnetic zirconium oxide nanocomposite as a catalyst for reduction of methylene blue. *SN Appl Sci* 2(7):1–8
8. Liu M, Zhang X, Li Z, Qu L, Han R (2020) Fabrication of zirconium (IV)-loaded chitosan/Fe₃O₄/graphene oxide for efficient removal of alizarin red from aqueous solution. *Carbohydr Polym* 248:116792
9. Suhail B, Bajpai S K, D' Souza A (2020) Microwave assisted facile green synthesis of carrageenan carbon dots (CDs) and their interaction with *Hibiscus Rosa sinensis* leaf cells. *Int J Environ Anal Chem* 1–17
10. Park YR, Jeong HY, Seo YS, Choi WK, Hong YJ (2017) Quantum-dot light-emitting diodes with nitrogen-doped carbon nanodot hole transport and electronic energy transfer layer. *Sci Rep* 7:46422
11. Das P, Ganguly S, Agarwal T, Maity P, Ghosh S, Choudhary S et al (2019) Heteroatom doped blue luminescent carbon dots as a nano-probe for targeted cell labeling and anticancer drug delivery vehicle. *Mater Chem Phys* 237:121860
12. Zhou Y, Zahran EM, Quiroga BA, Perez J, Mintz KJ, Peng Z et al (2019) Size-dependent photocatalytic activity of carbon dots with surface-state determined photoluminescence. *Appl Catal B* 248:157–166
13. Boakye-Yiadom KO, Kesse S, Opoku-Damoah Y, Filli MS, Aquib M, Joelle MMB et al (2019) Carbon dots: applications in bioimaging and theranostics. *Int J Pharm* 564:308–317
14. Barati A, Shamsipur M, Abdollahi H (2016) Metal-ion-mediated fluorescent carbon dots for indirect detection of sulfide ions. *Sens Actuators B Chem* 230:289–297
15. Yahaya Pudza M, Zainal Abidin Z, Abdul Rashid S, Md Yasin F, Noor A, Issa MA (2020) Eco-friendly sustainable fluorescent carbon dots for the adsorption of heavy metal ions in aqueous environment. *Nanomaterials* 10(2):315
16. Tabaraki R, Abdi O (2018) Green and simple turn off/on fluorescence sensor for mercury (II), cysteine and histidine. *J Mol Liq* 251:77–82
17. Di J, Xia J, Ji M, Wang B, Yin S, Xu H et al (2016) Carbon quantum dots induced ultrasmall BiOI nanosheets with assembled hollow structures for broad spectrum photocatalytic activity and mechanism insight. *Langmuir* 32(8):2075–2084
18. Huang Y, Liang Y, Rao Y, Zhu D, Cao J-j, Shen Z et al (2017) Environment-friendly carbon quantum dots/ZnFe₂O₄ photocatalysts: characterization biocompatibility and mechanisms for NO removal. *Environ Sci Technol* 51(5):2924–2933
19. Wang J, Han F, Rao Y, Hu T, Huang Y, Cao J-j et al (2018) Visible-light-driven nitrogen-doped carbon quantum dots/CaTiO₃ composite catalyst with enhanced NO adsorption for NO removal. *Ind Eng Chem Res* 57(31):10226–10233
20. Mahmood A, Shi G, Wang Z, Rao Z, Xiao W, Xie X et al (2020) Carbon quantum dots-TiO₂ nanocomposite as an efficient photocatalyst for the photodegradation of aromatic ring-containing mixed VOCs: an experimental and DFT studies of adsorption and electronic structure of the interface. *J Hazard Mater* 401:123402
21. Sahiner N, Suner SS, Sahiner M, Silan C (2019) Nitrogen and sulfur doped carbon dots from amino acids for potential biomedical applications. *J Fluorescence* 29(5):1191–1200
22. Zeng Y-W, Ma D-K, Wang W, Chen J-J, Zhou L, Zheng Y-Z et al (2015) N, S co-doped carbon dots with orange luminescence synthesized through polymerization and carbonization reaction of amino acids. *Appl Surf Sci* 342:136–143
23. Man Y, Li Z, Kong W-L, Li W, Dong W, Wang Y et al (2020) Starch fermentation wastewater as a precursor to prepare S, N-doped carbon dots for selective Fe (III) detection and carbon microspheres for solution decolorization. *Microchem J* 159:105338
24. Qin S, Yu X, Xu L (2021) Amplified fluorescence detection and adsorption of Au³⁺ by the fluorescent melamine formaldehyde microspheres incorporated with N and S co-doped carbon dots. *J Hazardous Mater* 405:123978
25. Zhao D, Feng J, Huo Q, Melosh N, Fredrickson GH, Chmelka BF et al (1998) Triblock copolymer syntheses of mesoporous silica with periodic 50 to 300 angstrom pores. *Science* 279(5350):548–552
26. Arends IW, Sheldon RA, Wallau M, Schuchardt U (1997) Oxidative transformations of organic compounds mediated by redox molecular sieves. *Angew Chem Int Ed Engl* 36(11):1144–1163
27. Gholamian F, Hajjami M (2019) Functionalization of hexagonal mesoporous silicas (HMS) for the synthesis of efficient catalyst and investigation of its catalytic activity in the synthesis of 1-amidoalkyl-2-naphthols and 2-substituted benzimidazoles. *React Kinet Mech Catal* 128(2):867–884
28. Nuntang S, Yousatit S, Yokoi T, Ngamcharussrivichai C (2019) Tunable mesoporosity and hydrophobicity of natural rubber/hexagonal mesoporous silica nanocomposites. *Microporous Mesoporous Mater* 275:235–243
29. Jadhav NV, Vavia PR (2017) Dodecylamine template-based hexagonal mesoporous silica (HMS) as a carrier for improved oral delivery of fenofibrate. *AAPS Pharm Sci Tech* 18(7):2764–2773
30. Ni P, Li Q, Xu C, Lai H, Bai Y, Chen T (2019) Optical properties of nitrogen and sulfur co-doped carbon dots and their applicability as fluorescent probes for living cell imaging. *Appl Surf Sci* 494:377–383
31. Marrakchi F, Hameed B, Bouaziz M (2020) Mesoporous and high-surface-area activated carbon from defatted olive cake by-products of olive mills for the adsorption kinetics and isotherm of methylene blue and acid blue 29. *J Environ Chem Eng* 8:104199
32. Iranzad F, Gheibi M, Eftekhari M (2018) Synthesis and application of polythiophene-coated Fe₃O₄ nanoparticles for preconcentration of ultra-trace levels of cadmium in different real samples followed by electrothermal atomic absorption spectrometry. *Int J Environ Anal Chem* 98(1):16–30
33. Liu Y, Jiang L, Li B, Fan X, Wang W, Liu P et al (2019) Nitrogen doped carbon dots: mechanism investigation and their

- application for label free CA125 analysis. *J Mater Chem B* 7(19):3053–3058
34. Ding C, Deng Z, Chen J, Jin Y (2020) One-step microwave synthesis of N, S co-doped carbon dots from 1, 6-hexanediamine dihydrochloride for cell imaging and ion detection. *Coll Surf B* 189:110838
35. Sun D, Ban R, Zhang P-H, Wu G-H, Zhang J-R, Zhu J-J (2013) Hair fiber as a precursor for synthesizing of sulfur-and nitrogen-co-doped carbon dots with tunable luminescence properties. *Carbon* 64:424–434
36. Song T, Zhao Y, Wang T, Li J, Jiang Z, Yang P (2020) Carbon dots doped with N and S towards controlling emitting. *J Fluorescence* 30(1):81–89
37. Smith AM, Nie S (2010) Semiconductor nanocrystals: structure, properties, and band gap engineering. *Acc Chem Res* 43(2):190–200
38. Li Y, Zhao Y, Cheng H, Hu Y, Shi G, Dai L et al (2012) Nitrogen-doped graphene quantum dots with oxygen-rich functional groups. *J Am Chem Soc* 134(1):15–18
39. Clogston JD, Patri AK (2011) Zeta potential measurement. In: McNeil S (ed) Characterization of nanoparticles intended for drug delivery. *Methods in molecular biology (Methods and Protocols)*, vol 697. Humana Press. https://doi.org/10.1007/978-1-60327-198-1_6
40. DeOliveira E, Neri CR, Ribeiro AO, Garcia VS, Costa LL, Moura AO et al (2008) Hexagonal mesoporous silica modified with copper phthalocyanine as a photocatalyst for pesticide 2, 4-dichlorophenoxyacetic acid degradation. *J Colloid Interface Sci* 323(1):98–104
41. Yuzbashi S, Mousazadeh M, Ramezani N, Sid Kalal H, Sabour B (2020) Mesoporous zirconium–silica nanocomposite modified with heteropoly tungstophosphoric acid catalyst for ultra-deep oxidative desulfurization. *Appl Organomet Chem* 34(2):e5326
42. Kuzminska M, Kovalchuk TV, Backov R, Gaigneaux EM (2014) Immobilizing heteropolyacids on zirconia-modified silica as catalysts for oleochemistry transesterification and esterification reactions. *J Catal* 320:1–8
43. Meng LY, Zhai SR, Li S, Zhai B, An QD, Song XW (2014) Synthesis and characterization of tungstophosphoric acid/pentaethylenehexamine/ZrSBA-15 and its use in the selective oxidation of benzyl alcohol under solvent-free conditions. *Eur J Inorg Chem* 2014(14):2337–2344
44. Wang Z, Xu C, Lu Y, Wu F, Ye G, Wei G et al (2017) Visualization of adsorption: luminescent mesoporous silica-carbon dots composite for rapid and selective removal of U (VI) and in situ monitoring the adsorption behavior. *ACS Appl Mater Interfaces* 9(8):7392–7398
45. Wang X, Li X, Li X, Wang Y, Han Q, Li J (2020) Determination of 2, 4, 6-trinitrophenol by in-situ assembly of SBA-15 with multi-hydroxyl carbon dots. *Anal Chim Acta* 1098:170–180
46. Galangasha MM, Kolkasaraeia ZN, Ghavidasta A, Shirzad-Sibonic M (2018) Adsorption of Acid Red 114 by facile prepared magnetic amino-nano-adsorbent: kinetics, isotherms and thermodynamics studies. *Desalin Water Treat* 116:317–328
47. Khandaker S, Toyohara Y, Saha GC, Awual MR, Kuba T (2020) Development of synthetic zeolites from bio-slag for cesium adsorption: Kinetic, isotherm and thermodynamic studies. *J Water Process Eng* 33:101055
48. Jia Y, Ding L, Ren P, Zhong M, Ma J, Fan X (2020) Performances and Mechanism of Methyl Orange and Congo Red Adsorbed on the Magnetic Ion-Exchange Resin. *J Chem Eng Data* 65(2):725–736
49. Harrou A, Gharibi E, Nasri H, El Ouahabi M (2020) Thermodynamics and kinetics of the removal of methylene blue from aqueous solution by raw kaolin. *SN Appl Sci* 2(2):277
50. Akbari Z, Ghiaci M, Nezampour F (2018) Encapsulation of vanadium phosphorus oxide into TiO₂ matrix for selective adsorption of methylene blue from aqueous solution. *J Chem Eng Data* 63(10):3923–3932
51. Gamal A, Farha SA, Sallam H, Mahmoud G, Ismail L (2010) Kinetic study and equilibrium isotherm analysis of reactive dyes adsorption onto cotton fiber. *Nat Sci* 8(11):95–110
52. Chakraborty T, Islam M, Zaman S, Kabir A, Ghosh G (2020) Jute (*Corchorus olitorius*) stick charcoal as a low-cost adsorbent for the removal of methylene blue dye from aqueous solution. *SN Appl Sci* 2:1–10
53. Jawad AH, Mohammed IA, Abdulhameed AS (2020) Tuning of fly ash loading into chitosan-ethylene glycol diglycidyl ether composite for enhanced removal of reactive red 120 dye: optimization using the box-behnken design. *J Polym Environ* 28(10):2720–2733
54. Jawad AH, Mubarak NSA, Abdulhameed AS (2020) Tunable Schiff's base-cross-linked chitosan composite for the removal of reactive red 120 dye: Adsorption and mechanism study. *Int J Biol Macromol* 142:732–741
55. Sharma Y, Sinha A, Upadhyay S (2010) Characterization and adsorption studies of *Cocos nucifera* L. activated carbon for the removal of methylene blue from aqueous solutions. *J Chem Eng Data* 55(8):2662–2667
56. Elhadiri N, Bouchdoug M, Benchanaa M, Boussetta A. (2018) Optimization of preparation conditions of novel adsorbent from sugar scum using response surface methodology for removal of methylene blue. *J Chem*. Vol. 2018
57. Beyranvand NS, Samiey B, Tehrani AD, Soleimani K (2019) Graphene oxide-cellulose nanowhisker hydrogel nanocomposite as a novel adsorbent for methylene blue. *J Chem Eng Data* 64(12):5558–5570
58. Jawad AH, Abdulhameed AS, Mastuli MS (2020) Acid-fractionalized biomass material for methylene blue dye removal: a comprehensive adsorption and mechanism study. *J Taibah Univ Sci* 14(1):305–313
59. Hu M, Yan X, Hu X, Feng R, Zhou M (2019) Synthesis of silver decorated silica nanoparticles with rough surfaces as adsorbent and catalyst for methylene blue removal. *J Sol Gel Sci Technol* 89(3):754–763
60. Dutta D, Thakur D, Bahadur D (2015) SnO₂ quantum dots decorated silica nanoparticles for fast removal of cationic dye (methylene blue) from wastewater. *Chem Eng J* 281:482–490
61. Jaseela P, Garvasis J, Joseph A (2019) Selective adsorption of methylene blue (MB) dye from aqueous mixture of MB and methyl orange (MO) using mesoporous titania (TiO₂)–poly vinyl alcohol (PVA) nanocomposite. *J Mol Liq* 286:110908
62. Wang Y, Zhou Y, Jiang G, Chen P, Chen Z (2020) One-step fabrication of carbonaceous adsorbent from corncob for enhancing adsorption capability of methylene blue removal. *Sci Rep* 10(1):1–9
63. Jawad AH, Abdulhameed AS (2020) Mesoporous Iraqi red kaolin clay as an efficient adsorbent for methylene blue dye: adsorption kinetic, isotherm and mechanism study. *Surf Interfaces* 18:100422
64. Jawad AH, Abdulhameed AS (2020) Statistical modeling of methylene blue dye adsorption by high surface area mesoporous activated carbon from bamboo chip using KOH-assisted thermal activation. *Energy Ecol Environment* 5(6):456–469

Publisher's Note Springer Nature remains neutral with regard to jurisdictional claims in published maps and institutional affiliations.